MDPI

Impact of Pre-Patterned Structures on Features of Laser-Induced Periodic Surface Structures

Stella Maragkaki [1,*], Panagiotis C. Lingos [1], George D. Tsibidis [1,2] and George Deligeorgis [1,2] and Emmanuel Stratakis [1,2,*]

[1] Institute of Electronic Structure and Laser, Foundation for Research and Technology—Hellas, 71110 Heraklion, Crete, Greece; plingos@physics.uoc.gr (P.C.L.); tsibidis@iesl.forth.gr (G.D.T.); deligeo@iesl.forth.gr (G.D.)
[2] Department of Physics, University of Crete, 71003 Heraklion, Crete, Greece
*   Correspondence: marag@iesl.forth.gr (S.M.); stratak@iesl.forth.gr (E.S.)

Abstract: The efficiency of light coupling to surface plasmon polariton (SPP) represents a very important issue in plasmonics and laser fabrication of topographies in various solids. To illustrate the role of pre-patterned surfaces and impact of laser polarisation in the excitation of electromagnetic modes and periodic pattern formation, Nickel surfaces are irradiated with femtosecond laser pulses of polarisation perpendicular or parallel to the orientation of the pre-pattern ridges. Experimental results indicate that for polarisation parallel to the ridges, laser induced periodic surface structures (LIPSS) are formed perpendicularly to the pre-pattern with a frequency that is independent of the distance between the ridges and periodicities close to the wavelength of the excited SPP. By contrast, for polarisation perpendicular to the pre-pattern, the periodicities of the LIPSS are closely correlated to the distance between the ridges for pre-pattern distance larger than the laser wavelength. The experimental observations are interpreted through a multi-scale physical model in which the impact of the interference of the electromagnetic modes is revealed.

Keywords: LIPSS; ripples; pre-patterns; surface plasmons; ultrafast dynamics; laser ablation; Nickel

1. Introduction

In the past decades, femtosecond laser pulses have become an effective tool in laser processing due to their capacity in precise materials' micro/nano-fabrication with an remarkable contribution to advances in science, technology and industry [1–6]. One particular type of patterns comprising the Laser-Induced Periodic Surface Structures (LIPSS) [7–23] is the most common type of topography that can be fabricated via irradiation of solids' surfaces by Gaussian beams (see also in [1,22] and references therein). Various laser parameters are usually controlled to tailor not only the LIPSS sizes and periodicities, but also the complexity of the induced surface patterns. The energy dose, laser wavelength, fluence and laser polarisation state [1,24,25] are among those parameters that are usually modulated to control those features or even increase the complexity of the topographies and therefore allow fabrication of morphologies attained [1].

In principle, LIPSS formation originates from the interference of the incident light and an induced electromagnetic wave that is scattered from the solid surface due to the presence of inhomogeneities or roughness [9,26]. These electromagnetic effects efficiently explain the periodicity values and orientation of High Spatial Frequency LIPSS (HSFL) and Low Spatial Frequency LIPSS (LSFL) (see in [1,22] and references therein). On the other hand, as the LIPSS covered topography is the final step of a sequence of processes, a detailed investigation of complex multiscale physical mechanisms that include spatially modulated energy absorption from the material, electron excitation, relaxation processes phase transitions and resolidification is required [19,21,27]. On the other hand, the physical process that leads to the above topographies is based on the concept that upon relaxation

a thin molten layer appears on the surface if laser conditions allow a phase transition; due to the spatial temperature gradient in the layer, strong instabilities are generated that produce fluid movement (i.e., Marangoni effects) and eventually upon re-solidification LIPSS are formed [15,19,23,28–32]. Therefore, the formation of HSFL or LSFL originates from a combination of (i) electromagnetic mechanisms that account for the orientation and define the spatially modulated deposited/absorbed energy and (ii) hydrodynamic effects that determine the features of the final topography. By contrast, the underlying physical mechanism for the formation of other types of LIPSS such as the suprawavelength structures (which are coined as grooves [18,20] or spikes [20,33] is mostly attributed to hydrodynamic and ablation effects.

Although the importance of the laser parameters as well as the environmental conditions [34] on the LIPSS characteristics is well reported, few studies have been focused on the impact of irradiation of surfaces of enhanced roughness and the role of the excited surface electromagnetic waves on the induced LIPSS topography [13,26,35,36]. More specifically, given that an increased roughness which can be produced through a multipulse irradiation influences the wavelength of the excited electromagnetic surface waves (i.e., Surface plasmons) and therefore the LIPSS formation and features [19,29,37,38], it is important to investigate the extent to which a pre-patterned sub-micrometer sized surface is capable to guide topography changes. Therefore, elucidation of the impact of the pre-patterned structures on the generation of LIPSS can provide a better insight on the underlying physical mechanisms giving rise to controllability and repeatability of the process in different materials. In a previous study, on rippled structures on pre-patterned surfaces, Miyaji et al. [39] reported on nanostructure formation on the crests of diamondlike carbon pre-patterned films due to a preferential enhancement of localised electric fields in those regions. Similar studies have been reported where the characteristic properties of the nano-sized grating formation was attributed to the excitation of surface plasmon polaritons [40–43].

Despite the important results reported in previous works, there are still several unexplored issues that need to be addressed in order to understand thoroughly the process of LIPSS formation upon irradiation of pre-patterned surfaces. As surface plasmon wave propagation wavelength and direction is correlated with the periodicity and orientation, respectively, of the produced LIPSS, a prominent question is whether the pre-pattern interdistance affects their characteristics (i.e., shape and size). Similarly, as electromagnetic effects are strongly related with the spatial distribution of the absorbed energy, a detailed analysis of the role of the pulse-by-pulse topography change in the energy modulation and absorption is very important to determine the process to LIPSS formation [13]. In a recent study by Radko et al. [44], it was shown that the predominant mechanism that accounts for LIPSS formation, the excitation of Surface Plasmon Polaritons is dependent on the ridges period, height and number, and therefore electromagnetic effects need to be addressed properly. Similar conclusions had been inferred in other reports with respect to the role of the pre-pattern features on the LIPSS formation [45]. Furthermore, as the produced hydrothermal waves and re-solidification process will provide the features of the surface pattern, it is of importance to investigate how the pre-pattern interacts with the produced melt fluid during the phase transformation and the extent to which the ridges drive the molten material towards forming LIPSS.

Therefore, to fully understand the topography evolution upon irradiation of prepatterned surfaces and evaluate their impact on LIPSS characteristics, a combined experimental and theoretical approach is presented in this work. To this end, we report on the fs laser induced periodic surface structure formation on pre-patterned Nickel surfaces, featuring different periods and orientation. Furthermore, a detailed analysis of the electromagnetic modes that are developed on the different topographies as a result of the increase of the energy dose is performed to describe the interpulse surface morphology changes.

2. Materials and Methods

The formation of the periodic pre-patterns is induced through electron-beam lithography (EBL) using a method presented in Figure 1.
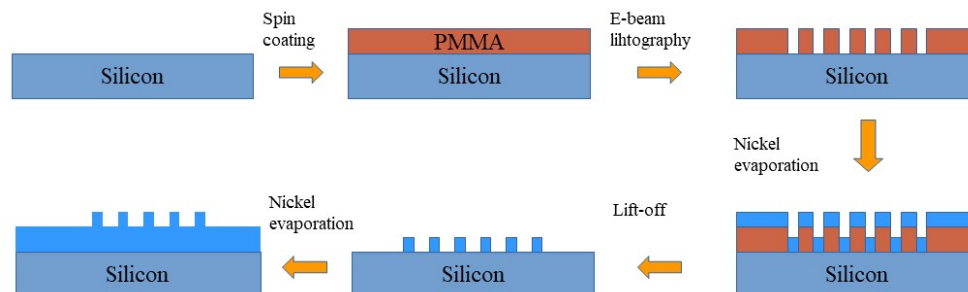

Figure 1. Schematic representation of the lift-off fabrication process.

A pristine silicon wafer (100 n-type 1–10 Ω cm) was used as the mechanical substrate. The desired patterns were defined using a Polymethyl methacrylate (PMMA) mask and e-beam lithography (RAITH Quantum combined with a JEOL 7000 F FESEM at 30 KVolts) was used to define a set of periodic structures consisting of lines (50% crest/50% depression) with a specific periodicity on each site. To ensure pattern fidelity, a proximity corrected dose pattern was used. Following PMMA development, 100 nm Nickel was evaporated and lift-off was used to define the Nickel lines. After lift-off, a blanket evaporation of 200 nm Nickel was used to realise the final Nickel structure that is 200 nm Nickel with 100 nm thick Nickel protrusions. The pattern fidelity is ensured by the directionality of the Nickel evaporation. The period was varied by changing the deposition pattern rastered by the electron beam during EBL, optimising the dose for each pattern in order to obtain the required dimensions. The pre-patterned surfaces were subsequently subjected to ultrashort pulsed-irradiation.For this purpose, the fundamental and the second harmonic (1026 nm and 513 nm) of an Yb:KGW laser system, delivering pulses of 170 fs pulse duration at 1 kHz repetition rate were used. Specifically, the Nickel sample is mounted on a *XYZ* translation stage normal to the incident laser beam, which is focused on the sample surface by a lens with 200 mm focal length. The pulse energy is adjusted by means of a variable attenuator formed by a half-waveplate and a polarising beam splitter. The fluence values were calculated as $\Phi_0 = 2E_P/\pi\,\omega_0^2$ with E_P the pulse energy and ω_0 the beam radius at $1/e^2$. Note that despite the pattern fidelity, a few random inhomogeneities due to surface pre-existing defects (i.e., defects on the fringes) can not always be avoided. For this reason the experiments have been repeated several times to ensure the reliability of the results. Following irradiation, the surface morphology was analyzed by means of field-emission scanning electron microscopy (SEM). The corresponding LIPSS periodicity of the induced structures was determined via the application of a two dimensional fast fourier transform (FFT) on the obtained SEM micrographs (see, e.g., Figure 2) through the use of the *Gwyddion* software. Each presented LIPSS periods is a product of multiple experiments conducted under identical conditions. The error bars shown in the plots below (Figures 3 and 4) are the outcome of these measurements.
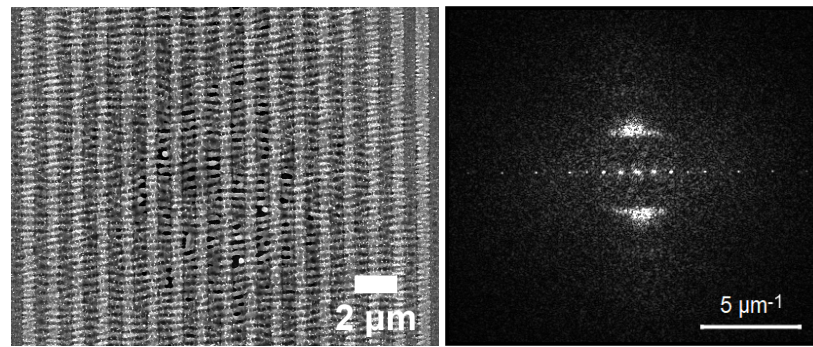
Figure 2. Pattern (**left**) with LIPSS periodicity measured through 2D-Fast Fourier Transform (**right**) on the SEM micrograph.
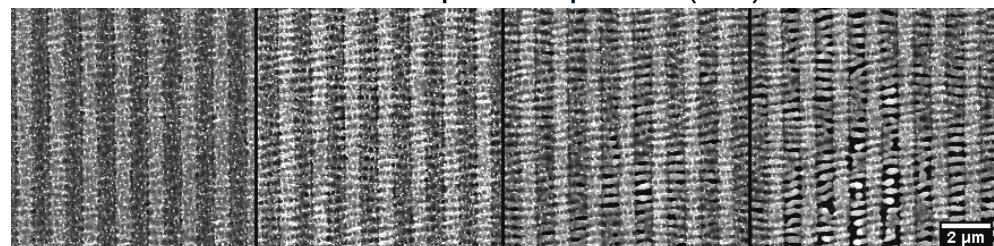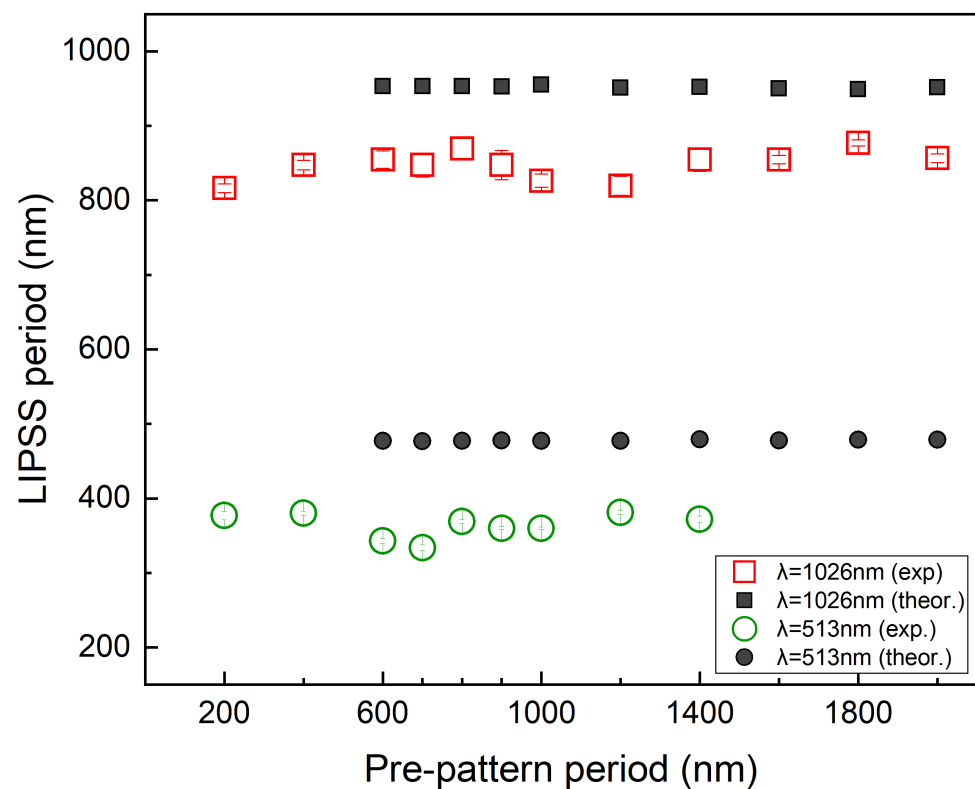

Figure 3. LIPSS spatial period as a function of pre-pattern periodicities. LIPSS on Nickel surfaces upon irradiation with 20 laser pulses (plot) with polarization parallel to the pre-pattern orientation. Experimental (*red* empty squares) and theoretical (*black* filled squares) values of the LIPSS periodicity upon irradiation with 1026 nm laser pulses. The experimental (*green* empty dots) and theoretical (*black* filled dots) values of the LIPSS periodicity upon irradiation with 513 nm laser pulses are also presented. The SEM micrographs below represent the evolution of LIPSS on pre-patterns with 1400 nm period upon irradiation with 4, 10, 15 and 20 pulses (from left to right), following irradiation with pulses of wavelength $\lambda = 513$ nm and peak fluence 0.12 J/cm^2).
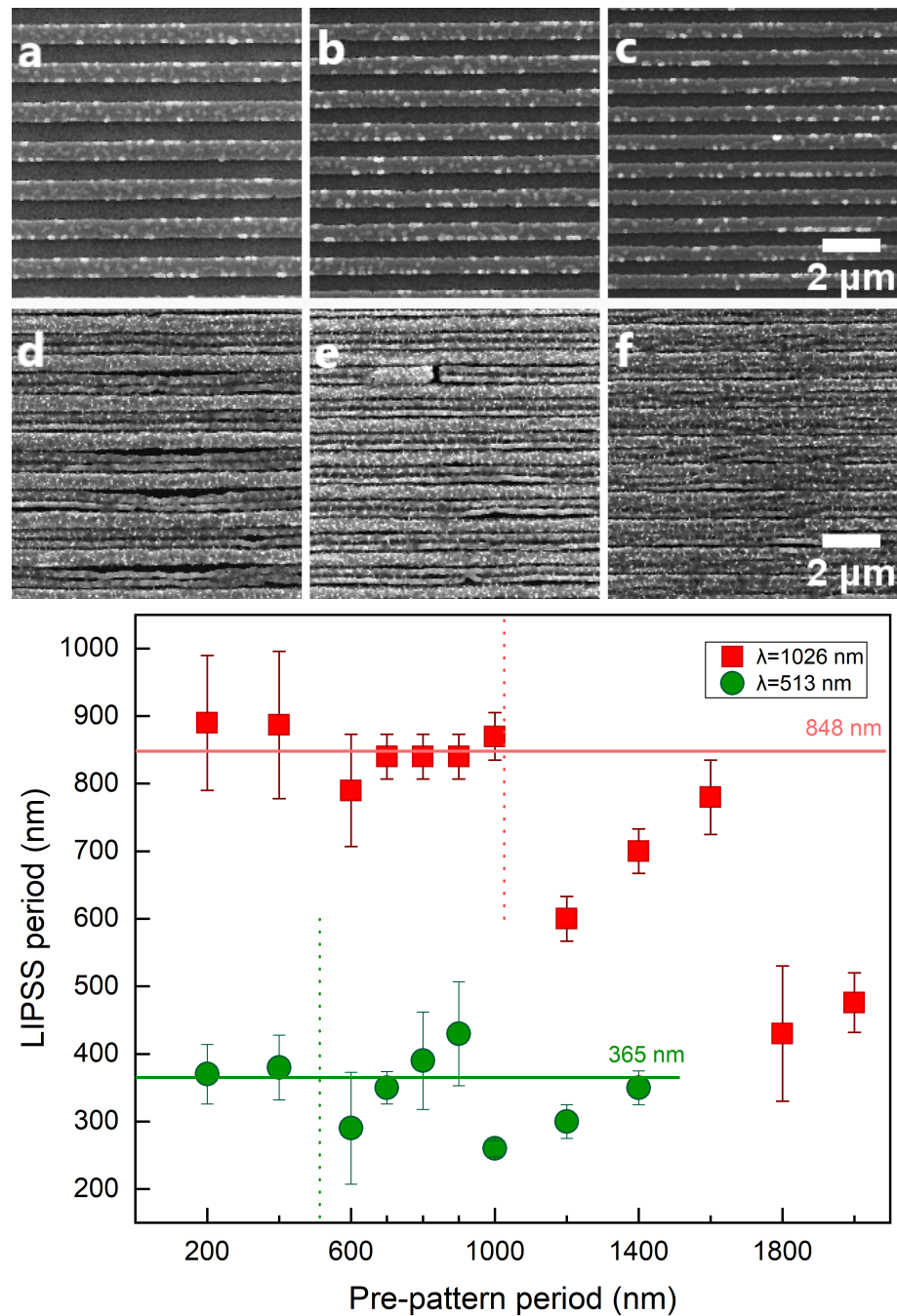
Figure 4. LIPSS on Nickel surfaces with different pre-pattern periodicities and a pre-pattern orientation perpendicular to the laser polarization. The SEM micrographs represent a comparison of non-irradiated pre-pattern structures (**a**–**c**) with periods 1400, 1200 and 1000 nm, respectively, and laser-induced ripples on the same pre-pattern structures with LIPSS period 350, 300 and 250 nm, respectively (**d**–**f**). The upper row (**a**–**c**) show the pre-pattern period and orientation. Laser parameters are the same for d, e and f. Femtosecond laser pulses with 513 nm laser wavelength, 25 laser pulses per spot and peak fluence at 0.12 J/cm^2 Irradiation with IR (filled squares) and visible (filled dots) fs laser pulses, with laser polarization perpendicular to the pre-pattern orientation. The vertical dotted lines represent the size of the laser wavelength. The horizontal lines correspond to the average LIPSS period when laser polarization is parallel to the pre-structures (see Figure 3). Here, LIPSS spatial period is independent of the pre-pattern spacing when the spacing is equal to or smaller than the laser wavelength. In contrast, at higher pre-pattern spacing, the pre-pattern has a great impact on the final LIPSS formation.

3. Results and Discussion

To reveal the role of the interaction of light to the excited surface plasmon waves in the process towards specific topography formation, we analysed the experimental findings for the periodicities of the induced LIPSS in various laser conditions and distances between the periodic pre-pattern arrangement. The LIPSS periods either remain independent of the periods of the pre-patterns or they are influenced by them. The latter case is an indication that the ridges topology itself tailors the interference of the electromagnetic modes that are excited. More specifically, the experimental results at both laser wavelengths (513 nm and 1026 nm) used, reveal the absence of any impact on the LIPSS periodicity. Indeed, as shown in Figure 3 when the pre-patterned arrangement has a direction parallel to the laser polarisation *E*, the final LIPSS period is constant and independent of the pre-patterned period. The discrepancy between the simulated (see next section) and experimental values is attributed to the precision in the estimation of the experimental conditions; however, a similar constant trend in the evolution is observed in both cases.

By contrast, when the laser polarisation is perpendicular to that of the pre-structures, there is a strong impact of the pre-pattern period on the final spatial topographies. In this case, the LIPSS period follows a distinct behaviour (Figure 4) that requires further investigation of the underlying physical processes involved. More specifically, for ridge distances of the size or slightly smaller than the laser wavelength, the LIPSS period appears to be close to the SPP wavelength. On the other hand, at larger pre-patterned distances, the LIPSS period is half the pre-pattern distance ($\Lambda_{LIPSS} = \Lambda_{pre-pattern}/2$).

Finally, for pre-patterns spacing which is substantially greater than the laser wavelength (almost twice as much as the laser wavelength) the correlation of the LIPSS period to the pre-pattern distance is provided by the following expression:

$$\Lambda_{LIPSS} = \frac{\Lambda_{pre-pattern}}{4} \tag{1}$$

The above observations are summarised in Table 1. It is evident that while the formation of LIPSS oriented perpendicularly to the periodic arrangement of ridges can be interpreted through the excitation of SPP along the direction of the pre-pattern (see simulated results below), the situation is more complex when the polarisation of the laser beam is perpendicular to the pre-pattern. To simulate the surface modification process, a multiscale description of the underlying physical mechanisms is used aiming also to interpret the interpulse topography changes.

Table 1. The final period of LIPSS as a function of the laser wavelength and the pre-pattern spacing. Final period remains unaffected on the surface topography when the pre-existing period is comparable to the laser wavelength. This table is valid when the laser polarisation is perpendicular to the pre-pattern period direction

λ (nm)	$\Lambda_{pre-pattern}$ (nm)	$\frac{\Lambda_{LIPSS}}{\Lambda_{pre-pattern}}$
1026	<1200	independent
1026	1200–1600	1/2
1026	≥1800	1/4
513	<600	independent
513	600–900	1/2
513	≥1000	1/4

3.1. Numerical Simulations

Given the experimentally attained distinct changes in the surface topography that depends on the laser polarisation direction, a detailed investigation of the electromagnetic effects is first elaborated; more specifically, it is known that scattering of light by a patterned or a corrugated surface is expected to reveal the characteristics of the induced surface

waves that operate as precursors of the final topography [9,21,44]. The interference of the incident beam with the surface waves leads to a spatial distribution of the energy that is absorbed from the material which in turn, excites the electron system [15,19,35,46]. A precise evaluation of the electromagnetic effects is performed through the employment of Finite Integration Technique (FIT) algorithms to solve Maxwell's equations using the commercial software CST Studio Suite. FIT [47,48] is a generalised finite difference scheme for the numerical solution of the Maxwell's equations in their integral form (Equation (2))

$$\oint_{\partial A} \mathbf{E} \cdot d\mathbf{s} = - \oiint_A \frac{d\mathbf{B}}{dt} \cdot d\mathbf{A} \tag{2a}$$

$$\oiint_V \mathbf{B} \cdot d\mathbf{A} = 0 \tag{2b}$$

$$\oint_{\partial A} \mathbf{H} \cdot d\mathbf{s} = \oiint_A (\frac{\partial \mathbf{D}}{\partial t} + \mathbf{J}) \cdot d\mathbf{A} \tag{2c}$$

$$\oiint_V \mathbf{D} \cdot d\mathbf{A} = \iiint_V \rho dV \tag{2d}$$

where the field and flux vectors are related to the material equations (Equation (3)),

$$\mathbf{B} = \mu\mathbf{H} + \mathbf{M} \tag{3a}$$

$$\mathbf{D} = \epsilon\mathbf{E} + \mathbf{P} \tag{3b}$$

$$\mathbf{J} = \sigma\mathbf{E} \tag{3c}$$

For a description of the variables in Equations (2) and (3), see in [47,48].

FIT provides reliable solutions for the entire range of electromagnetic field problems with complex geometries and shares similarities in accuracy with the widely used Finite Difference in the Time-Domain method (FDTD). FIT employs a pair of staggered grids, the primary grid and the dual grid such as the Yee cells in FDTD method. The primary grid composes the entire computational domain as a collection of volume cells V_i ($i = 1...n_V$) surrounded by facets A_i ($i = 1...n_A$) and edges L_i ($i = 1...n_L$). The dual grid is constructed so that each edge of the grid penetrates the surfaces of the other grid and each mesh point of one grid lies at the centre of the other grid. Each vector field and flux is converted in integral forms (scalars), the so called state variables. The calculation of material parameters is based on computing the integrals over the surface of the grid cells rather than on the definition of material data on grid points. The discretion form of the Maxwell equation's leads to a complete discrete set of matrix equations known as"Maxwell Grid Equations" representing integrations along edges and over facets of the grid. For a detailed description of FIT-technique, see in [49].

In order to elucidate the formation of LIPSS on a pre-patterned surface irradiated with a laser beam perpendicularly polarised with respect to the orientation of the ridges, a detailed investigation of the electromagnetic intensity distribution over the entire structure is required. Due to the symmetry of the pre-pattern along the Y axis, the problem can be reduced from a fully 3D to a quasi-2D focusing on one "unit-cell" of the pre-pattern with period $\Lambda_{pre-pattern}$. As the length of the pre-patterned structures in the Y direction surpasses the laser beam spot ($\approx$60 μm) and the beam spot radius is much greater than the studied pre-patterned periods in the experiments ($\Lambda_{pre-pattern} < 2$ μm), the laser field is simulated as a plane wave of wavelength λ = 1026 nm or 513 nm, linearly polarised along the X axis (perpendicular to the pre-pattern) or Y axis (parallel to the pre-pattern) irradiating the material at normal incidence. The geometry of the problem allows to keep the boundary conditions simple and the computational grid is terminated by two convolutional perfectly matched layers (convPML) in the Z direction to avoid non-physical reflections while periodic boundary conditions are used for X and Y directions. In order to capture the details of each pre-patterned surface, i.e., corrugations after irradiation and re-solidification, the grid cell dimensions are selected to be a fraction of the wavelength. In our simulations, we used 50 to 60 grid cells per wavelength applied in all directions.

The values of the refractive index n and extinction coefficient k for Nickel are based on fitting experimental data with a Lorentz–Drude model [50]. The pre-patterned structure consists of two 100 nm thick and $\Lambda_{pre-pattern}/4$ wide Nickel protrusions with spacing $\Lambda_{pre-pattern}/2$ between them. It is noted that the irradiated solid is thick enough to be considered optically as an nearly infinite layer (i.e., for the laser wavelengths used in the simulations $\lambda = 1026$ nm and $\lambda = 513$ nm, the skin depth of the Nickel is $\delta \approx 32$ nm and $\delta \approx 27$ nm, respectively). In our simulations, we computed the intensity $I = |\mathbf{E}|^2$, where $\mathbf{E}$ is the complex electric field, normalised by the maximum value I_0 emitted by the plane wave source.

A three-dimensional Two Temperature Model (TTM) is then applied to describe the energy transfer from the excited electron system to the lattice subsystem. To evaluate the influence of light on the evolving (i.e., pulse by pulse) topographies, a multi-physics approach is followed to numerically describe energy absorption, excitation, relaxation and phase transitions that eventually lead to an evolution of the irradiated pattern [15,17,51]. Due to fact that the lattice temperatures that are attained from the exposure of the solid to extreme laser conditions exceed the melting point of the material, a detailed investigation of the dynamics of the produced fluid is conducted to determine the morphological features of the final topography. A thorough description of the multiscale methodology used to simulate surface modification has been presented in several previous reports [15,19,23,24]. Below, results of the modelling approach are summarised that demonstrate the role of the direction of the polarisation beam, the influence of the characteristics of the electromagnetic modes and the impact of the pre-patterned period in the periodicity of the induced LIPSS. Simulations have been performed with pulse duration equal to $\tau_p = 170$ fs and peak fluence equal to 0.12 J/cm^2 and for different sizes of the pre-pattern periods $\Lambda_{pre-pattern} = 700$ nm, 1400 nm for $\lambda = 513$ nm and $\Lambda_{pre-pattern} = 700$ nm, 800 nm, 1900 nm and 1300 nm for $\lambda = 1026$ nm).

3.2. Laser Polarisation Parallel to the pre-pattern Orientation

The predominant electromagnetic process that accounts for the formation of LSFL structures is the excitation of surface plasmons waves (SPW) and interference with the incident beam [9]. In previous reports, it has been shown that SPW propagate in the direction of the laser polarisation [15,38] while their interference with the incident beam leads to a periodic energy deposition/absorption that result into the development of thermocapillary waves upon a phase transition. Upon re-solidification, those waves result into the formation of LIPSS that are oriented perpendicularly to the pre-pattern. Theoretical predictions shown in Figure 5 illustrate an upper view (Figure 5a) and side view (Figure 5b), respectively, of the induced pattern following irradiation with fifteen pulses. These simulations indicate that ripples are formed both on the pre-pattern and the region between the ridges which is confirmed from experimental observations (see Figure 3) for various number of pulses. The periodicity of the induced LIPSS is predicted to be independent of the $\Lambda_{pre-pattern}$ which is explained by the fact that the electromagnetic waves that propagate along the pre-patterned surface are not influenced by the distance of the ridges as they propagate in a direction parallel the patterns. To elucidate the role of the excitation and propagation of the electromagnetic waves in the formation of LIPSS, first, simulations have been performed to reveal the impact of the electromagnetic effects. To model the influence of the electromagnetic effects in the orientation and periodicity of the SPW, two strategies have been developed:

(i) The employment of Sipe's theory (see details in [9]) in which the efficacy η with which a surface roughness at the wavevector $\vec{K}$ (i.e., normalised wavevector $|\vec{K}| = \lambda/\Lambda$, where Λ stands for the predicted structural periodicity) induces inhomogeneous radiation absorption. The inhomogeneous energy deposition into the irradiated material is computed by the calculation of the product $\eta(\vec{K}, \vec{k_i}) \times |b(\vec{K})|$, where b represents a measure of the amplitude of the surface roughness at $\vec{K}$ and $\vec{k_i}$ stands for the component of the wave vector of the incident laser beam on the material's surface plane. In principle, surface roughness is

considered to be represented by spherically shaped islands and values from Sipe's theory for the 'shape' ($s = 0.4$) and the 'filling' ($f = 0.9$, for a 'rough' surface) factors are assumed. According to Sipe's theory, LIPSS are formed where η-maps exhibits sharp features (maxima or minima). The values for the dielectric parameter of the irradiated material used to calculate the efficacy factor are $\epsilon = -6.4292 + i10.656$ and $\epsilon = -18.464 + i29.038$ and for $\lambda = 513$ nm and $\lambda = 1026$ nm, respectively [50]. In Figure 5c, the efficacy factor is calculated for a laser beam at $\lambda = 513$ nm (similar results are inferred for $\lambda = 1026$ nm) polarised along the Y-axis and the sharp peak along $K_Y = \lambda/\Lambda_Y$ (*white* dashed line) indicates that the inhomogeneous (periodic) energy absorption has a preferential direction along the Y-axis; furthermore, the periodicity of the relevant surface waves is provided from the expression $\Lambda_Y = \lambda/|K_Y^0|$ where K_Y^0 corresponds to the position of the sharp point along the $|K_Y|$ direction.

(ii) An investigation has been performed based on the solution of Maxwell equations on the pre-patterned surface considering interference patterns as a result of light interaction with the scattered waves induced by randomly distributed hemispherical bumps of radius $R = 40$ nm. Simulation results in (Figure 5d) illustrate the resulting absorption maps resulting from the coherent response of the individual bumps for $\lambda = 513$ nm (similar results are inferred for $\lambda = 1026$ nm). The pattern shown in (Figure 5d) demonstrates the result of the interference of the laser field with the collective scattered surface waves below the pre-patterned surface. According to that analysis, the surface waves propagate along the Y-axis and they have periodicity Λ_Y close to the laser wavelength and similar to the value calculated in (i). This is also illustrated in Figure 5e that depicts the FFT analysis of Figure 5d.
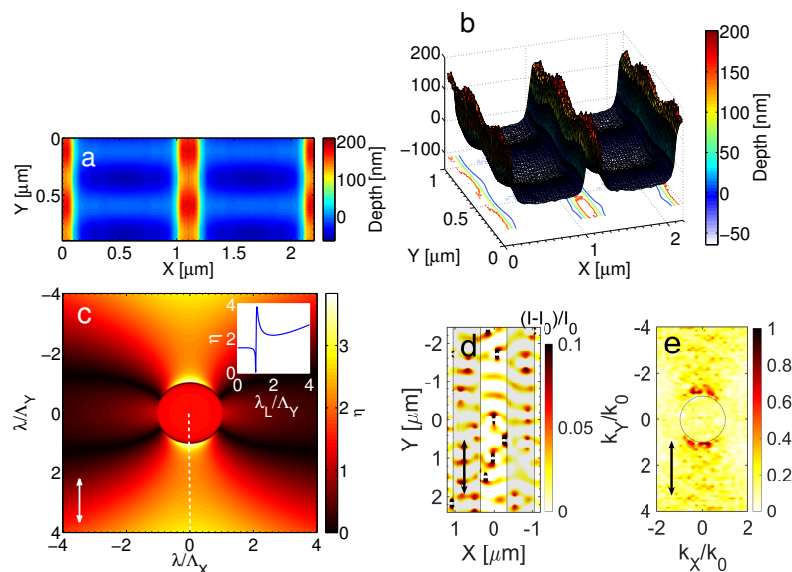

Figure 5. Topography following irradiation of Nickel with fifteen laser pulses: (**a**) upper view (at 1026 nm) and (**b**) side view (at 1026 nm). Polarisation is along the Y-axis. (**c**) Efficacy Factor map for LIPSS formation (at 513 nm); the inset shows η along the *white* dashed line (*white* double headed arrow indicates the laser polarisation direction). (**d**) Electromagnetic simulations that shows surface wave propagation direction and periodicity (at $\lambda = 513$ nm) on a XY-plane and the corresponding FFT (**e**); vertical shaded regions indicate the position of the prepatterned ridges. The periodicity of the scattered waves (far fields) is equal to $\Lambda_Y(=2\pi/k_Y)$ and they are captured in the FFT figure where $k_0 = 2\pi/\lambda$ is the free-space wavevector (*black* double headed arrow indicates the laser polarisation direction).

3.3. Laser Polarisation Perpendicular to the pre-pattern Orientation

By contrast, a more complex scenario occurs when the laser polarisation is perpendicular to the ridges orientation.

To examine whether the electromagnetic factor influences the spatial distribution of the energy accumulation on the pre-patterned surface for different $\Lambda_{pre-pattern}$, numerical calculations have been performed to evaluate the impact of the pre-pattern in the energy absorption. For the sake of simplicity, simulations are restricted to the investigation of the topography interpulse changes for four pulses that is expected to capture the pattern periodicities of the produced morphology. In Figures 6 and 7, the evolution of topographies are illustrated as a function of $\Lambda_{pre-pattern}$ and λ. Electromagnetic simulations show the spatial distribution of the electromagnetic field on a pre-pattern surface in one period. Theoretical results indicate that assuming energy absorption for pre-patterns periodicities larger than twice the laser wavelength, two hills are formed inside the valley that are $\Lambda_{pre-pattern}/4$ apart (Figure 6e–h,m–p), which is explained by the interference of the electromagnetic waves that are excited on the ridges. By contrast, at smaller inter-pattern periodicities, one hill is produced at the centre of the valley (Figure 6a–d,i–l), which is again pertinent to the behaviour of the excited electromagnetic modes. Furthermore, for pre-pattern distances of the size of the laser wavelength, topographies of periodicity *independent* of $\Lambda_{pre-pattern}$ are fabricated and periodic structures of the size of the excited SPP is produced (Figure 7). Such periodicities have been observed experimentally and predicted from theoretical models in various other previous reports (see in [1] and references therein).
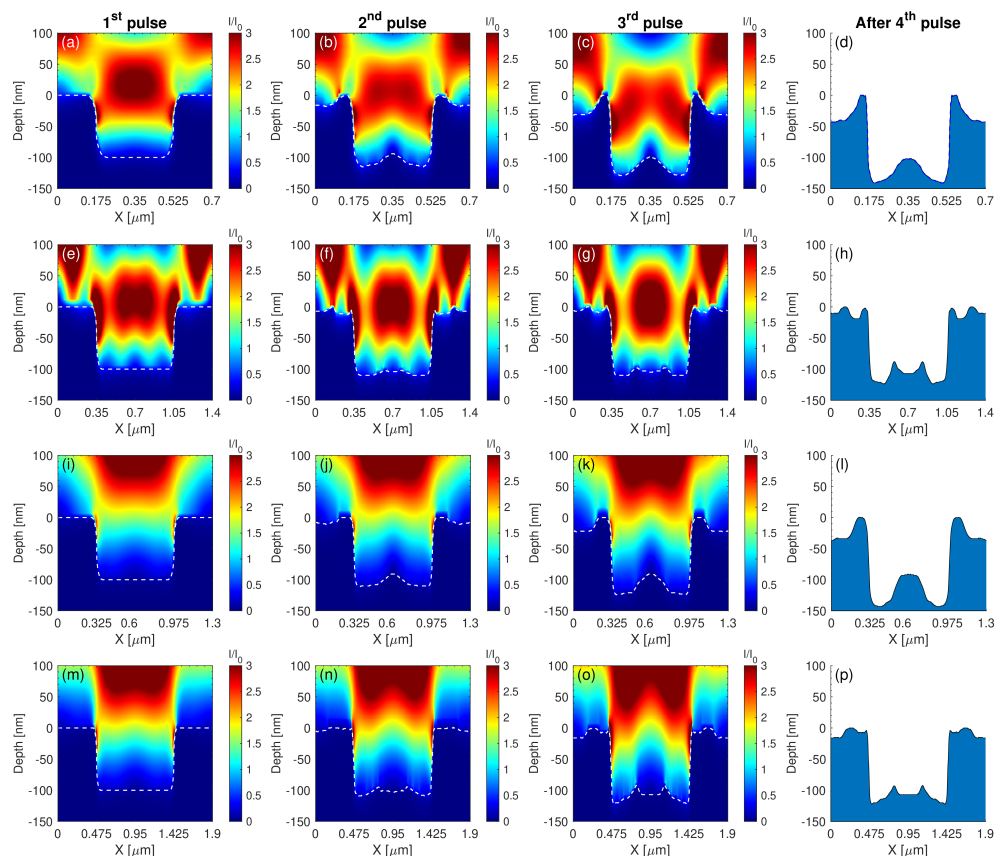

Figure 6. Spatial profile of the intensity distribution for different pre-pattern distances $\Lambda_{pre-pattern}$ and laser wavelengths λ on the *x-z* plane. In these images the pre-pattern topography evolution upon successive irradiation is also captured (*white* dashed lines). The first, second and third column represent the intensity distribution during the first, second and third laser pulse, respectively, while the final LIPSS topography after four pulses is depicted in the fourth column (side view of the morphology). (**a–d**) $\lambda = 513$ nm for $\Lambda_{pre-pattern} = 700$ nm, (**e–h**) $\lambda = 513$ nm for $\Lambda_{pre-pattern} = 1400$ nm, (**i–l**) $\lambda = 1026$ nm for $\Lambda_{pre-pattern} = 1300$ nm and (**m–p**) $\lambda = 1026$ nm for $\Lambda_{pre-pattern} = 1900$ nm. The *white* dashed line indicates the surface boundary.
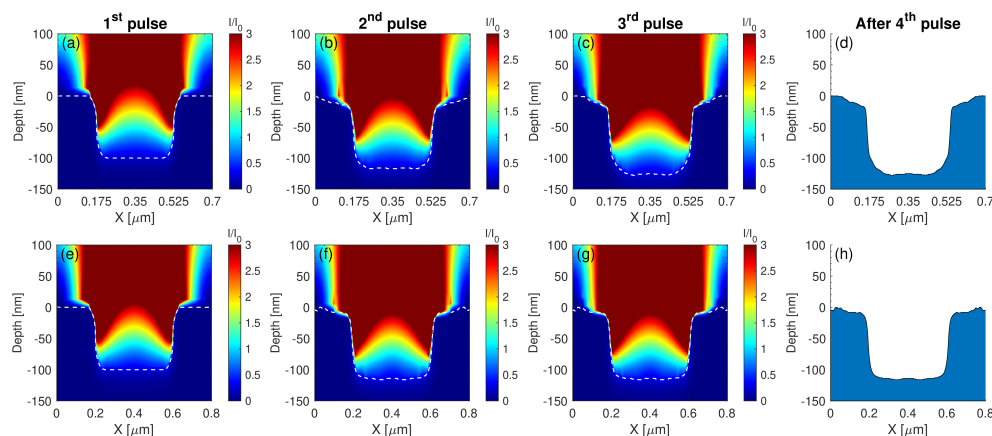
Figure 7. Spatial profile of the intensity distribution for different pre-pattern distances (**a**–**c**) $\Lambda_{pre-pattern} = 700$ nm and (**e**–**g**) $\Lambda_{pre-pattern} = 800$ nm during three successive irradiations with laser pulses of $\lambda = 1026$ nm and the corresponding final topographies (**d**,**h**) after the fourth pulse. The *white* dashed line indicates the surface boundary.

The above investigation and results define a methodology to enhance the efficiency of coupling of the electromagnetic modes that are excited with the incident beam which demonstrates, conclusively, the impact of the geometrical characteristics of the pre-patterned surface on the periodicities and orientation of the induced LIPSS. More specifically, the constructive interference that is caused in the case of irradiation with polarised beam perpendicularly to the ridge orientation could be used to produce LIPSS of variable periodicity by modulating the distance between the pre-patterns. The capability to control and optimise the periodicity of a rippled pattern and fabrication nano/micro size topographies by regulating the pattern features and laser polarisation can provide unique opportunities for promising biosensing or plasmonic applications.

4. Conclusions

In summary, we have investigated experimentally and numerically the efficiency of SPP excitation on periodic sets of ridges of Nickel surfaces. The laser parameters, such as the polarisation and wavelength and the pre-pattern features (i.e., orientation with respect to the laser polarisation and distance between ridges) were varied and LIPSS were fabricated with periodicities ranging between $\sim\Lambda_{pre-pattern}/4$ and $\sim\lambda$ which are dependent on the polarisation of the incident beam and the periodicity of the ridge arrangement. The detailed analysis of the LIPSS formation in different conditions and ridge distances through the evaluation of the electromagnetic effects and the incorporation of a multiscale physical modelling approach and experimental validation can set the basis for control of the parameters to fabricate patterns with desired properties for a wide range of optoelectronic applications.

References

1. Stratakis, E.; Bonse, J.; Heitz, J.; Siegel, J.; Tsibidis, G.D.; Skoulas, E.; Papadopoulos, A.; Mimidis, A.; Joel, A.C.; Comanns, P.; et al. Laser engineering of biomimetic surfaces. *Mater. Sci. Eng. R Rep.* **2020**, *141*, 100562. [CrossRef]
2. Vorobyev, A.Y.; Guo, C. Direct femtosecond laser surface nano/microstructuring and its applications. *Laser Photonics Rev.* **2013**, *7*, 385–407. [CrossRef]
3. Zorba, V.; Stratakis, E.; Barberoglou, M.; Spanakis, E.; Tzanetakis, P.; Anastasiadis, S.H.; Fotakis, C. Biomimetic Artificial Surfaces Quantitatively Reproduce the Water Repellency of a Lotus Leaf. *Adv. Mater.* **2008**, *20*, 4049–4054. [CrossRef]
4. Zorba, V.; Persano, L.; Pisignano, D.; Zorba, V.; Persano, L.; Pisignano, D.; Athanassiou, A.; Stratakis, E.; Cingolani, R.; Tzanetakis, P.; et al. Making silicon hydrophobic: Wettability control by two-lengthscale simultaneous patterning with femtosecond laser irradiation. *Nanotechnology* **2006**, *17*, 3234–3238. [CrossRef]
5. Diels, J.C.; Rudolph, W. *Ultrashort Laser Pulse Phenomena*; Elsevier: Amsterdam, The Netherlands, 2006.
6. Papadopoulou, E.L.; Samara, A.; Barberoglou, M.; Manousaki, A.; Pagakis, S.N.; Anastasiadou, E.; Fotakis, C.; Stratakis, E. Silicon Scaffolds Promoting Three-Dimensional Neuronal Web of Cytoplasmic Processes. *Tissue Eng. Part C Methods* **2009**, *16*, 497–502. [CrossRef]
7. Birnbaum, M. Semiconductor surface damage produced by Ruby lasers. *J. Appl. Phys.* **1965**, *36*, 3688–3689. [CrossRef]
8. Guosheng, Z.; Fauchet, P.M.; Siegman, A.E. Growth of spontaneous periodic surface structures on solids during laser illumination. *Phys. Rev. B* **1982**, *26*, 5366. [CrossRef]
9. Sipe, J.E.; Young, J.F.; Preston, J.S.; Driel, H.M.v. Laser-induced periodic surface structure. I. Theory. *Phys. Rev. B* **1983**, *27*, 1141. [CrossRef]
10. Shimotsuma, Y.; Kazansky, P.G.; Qiu, J.; Hirao, K. Self-organized nanogratings in glass irradiated by ultrashort light pulses. *Phys. Rev. Lett.* **2003**, *91*, 247405. [CrossRef] [PubMed]
11. Bonse, J.; Munz, M.; Sturm, H. Structure formation on the surface of indium phosphide irradiated by femtosecond laser pulses. *J. Appl. Phys.* **2005**, *97*, 013538. [CrossRef]
12. Varlamova, O.; Costache, F.; Reif, J.; Bestehorn, M. Self-organized pattern formation upon femtosecond laser ablation by circularly polarized light. *Appl. Surf. Sci.* **2006**, *252*, 4702–4706. [CrossRef]
13. Huang, M.; Zhao, F.; Cheng, Y.; Xu, N.; Xu, Z. Origin of laser-induced near-subwavelength ripples: Interference between surface plasmons and incident laser. *ACS Nano* **2009**, *3*, 4062–4070. [CrossRef]
14. Stratakis, E.; Ranella, A.; Fotakis, C. Biomimetic micro/nanostructured functional surfaces for microfluidic and tissue engineering applications. *Biomicrofluidics* **2011**, *5*, 013411. [CrossRef]
15. Tsibidis, G.D.; Barberoglou, M.; Loukakos, P.A.; Stratakis, E.; Fotakis, C. Dynamics of ripple formation on silicon surfaces by ultrashort laser pulses in subablation conditions. *Phys. Rev. B* **2012**, *86*, 115316. [CrossRef]
16. Tsibidis, G.D.; Stratakis, E.; Aifantis, K.E. Erratum: "Thermoplastic deformation of silicon surfaces induced by ultrashort pulsed lasers in submelting conditions". *J. Appl. Phys.* **2012**, *112*, 089901. [CrossRef]
17. Derrien, T.J.Y.; Itina, T.E.; Torres, R.; Sarnet, T.; Sentis, M. Possible surface plasmon polariton excitation under femtosecond laser irradiation of silicon. *J. Appl. Phys.* **2013**, *114*, 083104. [CrossRef]
18. Nivas, J.J.; He, S.; Rubano, A.; Vecchione, A.; Paparo, D.; Marrucci, L.; Bruzzese, R.; Amoruso, S. Direct Femtosecond Laser Surface Structuring with Optical Vortex Beams Generated by a q-plate. *Sci. Rep.* **2015**, *5*, 17929. [CrossRef] [PubMed]
19. Tsibidis, G.D.; Fotakis, C.; Stratakis, E. From ripples to spikes: A hydrodynamical mechanism to interpret femtosecond laser-induced self-assembled structures. *Phys. Rev. B* **2015**, *92*, 041405. [CrossRef]
20. Tsibidis, G.D.; Skoulas, E.; Papadopoulos, A.; Stratakis, E. Convection roll-driven generation of supra-wavelength periodic surface structures on dielectrics upon irradiation with femtosecond pulsed lasers. *Phys. Rev. B* **2016**, *94*, 081305. [CrossRef]
21. Rudenko, A.; Colombier, J.P.; Itina, T.E. From random inhomogeneities to periodic nanostructures induced in bulk silica by ultrashort laser. *Phys. Rev. B* **2016**, *93*, 075427. [CrossRef]
22. Bonse, J.; Hohm, S.; Kirner, S.V.; Rosenfeld, A.; Kruger, J. Laser-Induced Periodic Surface Structures-A Scientific Evergreen. *IEEE J. Sel. Top. Quantum Electron.* **2017**, *23*, 9000615. [CrossRef]
23. Rudenko, A.; Colombier, J.P.; Höhm, S.; Rosenfeld, A.; Krüger, J.; Bonse, J.; Itina, T.E. Spontaneous periodic ordering on the surface and in the bulk of dielectrics irradiated by ultrafast laser: A shared electromagnetic origin. *Sci. Rep.* **2017**, *7*, 12306. [CrossRef]
24. Tsibidis, G.D.; Skoulas, E.; Stratakis, E. Ripple formation on nickel irradiated with radially polarized femtosecond beams. *Opt. Lett.* **2015**, *40*, 5172. [CrossRef] [PubMed]
25. Skoulas, E.; Manousaki, A.; Fotakis, C.; Stratakis, E. Biomimetic surface structuring using cylindrical vector femtosecond laser beams. *Sci. Rep.* **2017**, *7*, 45114. [CrossRef]

26.　Rudenko, A.; Mauclair, C.; Garrelie, F.; Stoian, R.; Colombier, J.P. Light absorption by surface nanoholes and nanobumps. *Appl. Surf. Sci.* **2019**, *470*, 228–233. [CrossRef]

27.　Rethfeld, B.; Ivanov, D.S.; Garcia, M.E.; Anisimov, S.I. Modelling ultrafast laser ablation. *J. Phys. D Appl. Phys.* **2017**, *50*, 193001. [CrossRef]

28.　Gurevich, E.L. Mechanisms of femtosecond LIPSS formation induced by periodic surface temperature modulation. *Appl. Surf. Sci.* **2016**, *374*, 56–60. [CrossRef]

29.　Tsibidis, G.D.; Mimidis, A.; Skoulas, E.; Kirner, S.V.; Krüger, J.; Bonse, J.; Stratakis, E. Modelling periodic structure formation on 100Cr6 steel after irradiation with femtosecond-pulsed laser beams. *Appl. Phys. A* **2017**, *124*, 27. [CrossRef]

30.　Tsibidis, G.D.; Stratakis, E. Ionisation processes and laser induced periodic surface structures in dielectrics with mid-infrared femtosecond laser pulses. *Sci. Rep.* **2020**, *10*, 8675. [CrossRef] [PubMed]

31.　Zhang, D.; Ranjan, B.; Tanaka, T.; Sugioka, K. Carbonized Hybrid Micro/Nanostructured Metasurfaces Produced by Femtosecond Laser Ablation in Organic Solvents for Biomimetic Antireflective Surfaces. *ACS Appl. Nano Mater.* **2020**, *3*, 1855–1871. [CrossRef]

32.　Zhang, D.; Liu, R.; Li, Z. Irregular LIPSS produced on metals by single linearly polarized femtosecond laser. *Int. J. Extrem. Manuf.* **2021**, *4*, 015102. [CrossRef]

33.　Zuhlke, C.A.; Anderson, T.P.; Alexander, D.R. Formation of multiscale surface structures on nickel via above surface growth and below surface growth mechanisms using femtosecond laser pulses. *Opt. Express* **2013**, *21*, 8460. [CrossRef]

34.　Maragkaki, S.; Elkalash, A.; Gurevich, E. Orientation of ripples induced by ultrafast laser pulses on copper in different liquids. *Appl. Phys. A Mater. Sci. Process.* **2017**, *123*, 721. [CrossRef]

35.　Tsibidis, G.D.; Stratakis, E. Ripple formation on silver after irradiation with radially polarised ultrashort-pulsed lasers. *J. Appl. Phys.* **2017**, *121*, 163106. [CrossRef]

36.　Liu, R.; Zhang, D.; Li, Z. Femtosecond laser induced simultaneous functional nanomaterial synthesis, in situ deposition and hierarchical LIPSS nanostructuring for tunable antireflectance and iridescence applications. *J. Mater. Sci. Technol.* **2021**, *89*, 179–185. [CrossRef]

37.　Rudenko, A.; Mauclair, C.; Garrelie, F.; Stoian, R.; Colombier, J.P. Self-organization of surfaces on the nanoscale by topography-mediated selection of quasi-cylindrical and plasmonic waves. *Nanophotonics* **2019**, *8*, 459–465. [CrossRef]

38.　Bonse, J.; Rosenfeld, A.; Krüger, J. On the role of surface plasmon polaritons in the formation of laser-induced periodic surface structures upon irradiation of silicon by femtosecond-laser pulses. *J. Appl. Phys.* **2009**, *106*, 104910. [CrossRef]

39.　Miyaji, G.; Miyazaki, K. Nanoscale ablation on patterned diamondlike carbon film with femtosecond laser pulses. *Appl. Phys. Lett.* **2007**, *91*, 123102. [CrossRef]

40.　Miyazaki, K.; Miyaji, G. Nanograting formation through surface plasmon fields induced by femtosecond laser pulses. *J. Appl. Phys.* **2013**, *114*, 153108. [CrossRef]

41.　Miyazaki, K.; Miyaji, G.; Inoue, T. Nanograting formation on metals in air with interfering femtosecond laser pulses. *Appl. Phys. Lett.* **2015**, *107*, 071103. [CrossRef]

42.　Miyaji, G.; Miyazaki, K. Fabrication of 50-nm period gratings on GaN in air through plasmonic near-field ablation induced by ultraviolet femtosecond laser pulses. *Opt. Express* **2016**, *24*, 4648–4653. [CrossRef] [PubMed]

43.　Miyaji, G.; Tamamura, Y. Structural coloration of a stainless steel surface with homogeneous nanograting formed by femtosecond laser ablation. *Opt. Mater. Express* **2019**, *9*, 2902–2909. [CrossRef]

44.　Radko, I.P.; Bozhevolnyi, S.I.; Brucoli, G.; Martín-Moreno, L.; García-Vidal, F.J.; Boltasseva, A. Efficiency of local surface plasmon polariton excitation on ridges. *Phys. Rev. B Condens. Matter Mater. Phys.* **2008**, *78*, 115115. [CrossRef]

45.　Fraggelakis, F.; Tsibidis, G.D.; Stratakis, E. Tailoring submicrometer periodic surface structures via ultrashort pulsed direct laser interference patterning. *Phys. Rev. B* **2021**, *103*, 54105. [CrossRef]

46.　Gaković, B.; Tsibidis, G.D.; Skoulas, E.; Petrović, S.M.; Vasić, B.; Stratakis, E. Partial ablation of Ti/Al nano-layer thin film by single femtosecond laser pulse. *J. Appl. Phys.* **2017**, *122*, 223106. [CrossRef]

47.　Weiland, T. A Discretization Method for the Solution of Maxwell's Equations for Six-Component Fields. *Electron. Commun.* **1977**, *31*, 116–120.

48.　Clemens, M.; Weiland, T. Discrete Electromagnetism with the Finite Integration Technique. *Prog. Electromagn. Res.* **2001**, *32*, 65–87. [CrossRef]

49.　Carstensen, C.; Funken, S.; Hackbusch, W.; Hoppe, R.W.; Monk, P. *Computational Electromagnetics*; Springer: Berlin/Heidelberg, Germany, 2003; pp. 183–196. [CrossRef]

50.　Rakić, A.D.; Djurišić, A.B.; Elazar, J.M.; Majewski, M.L. Optical properties of metallic films for vertical-cavity optoelectronic devices. *Appl. Opt.* **1998**, *37*, 5271–5283. [CrossRef]

51.　Anisimov, S.I.; Kapeliovich, B.L.; Perelman, T.L.; Anisimov, S.I.; Kapeliovich, B.L.; Perelman, T.L. Electron emission from metal surfaces exposed to ultrashort laser pulses. *Sov. Phys. JETP* **1974**, *39*, 375–377.